


Onset of Rayleigh-Bénard convection in dielectric liquids with electric conduction

Yuxing Peng ^{1,2}, R. Deepak Selvakumar ³, and Jian Wu ^{1,2,*}

¹*School of Energy Science and Engineering, Harbin Institute of Technology, Harbin 150001, People's Republic of China*

²*Heilongjiang Key Laboratory of Micro- and Nano-scale Fluid Flow and Heat Transfer, Harbin Institute of Technology, Harbin 150001, People's Republic of China*

³*Department of Mechanical and Nuclear Engineering, Khalifa University, Abu Dhabi 20009, UAE*



(Received 31 May 2023; accepted 8 November 2023; published 16 January 2024)

This paper presents a combined stability analysis and numerical investigation of Rayleigh-Bénard convection in a planar dielectric liquid layer subjected to the simultaneous action of Coulomb and buoyancy forces. For the first time, Rayleigh-Bénard convective instability with electric conduction is considered. Fully coupled set of governing equations for fluid flow, heat transfer, and electrostatics are solved using the finite-volume method (FVM) framework of OpenFOAM. The fluid layer is destabilized under the combined action of buoyancy and Coulomb forces. Rayleigh number (Ra) and the Conduction number (C_0) are the control parameters for fluid flow. Distributions of physical variables in the hydrostatic state are derived. Modal stability analysis is performed to establish the neutral stability curve in the Ra - C_0 plane. Present numerical results are compared with the results of stability analysis. The flow and heat transfer characteristics in the Ra - C_0 parameter space are analyzed. The present study provides deeper insights into the electrothermo-convective flow mechanism due to the EHD conduction phenomenon occurring at weak and medium electric fields. The results of this study can serve as a benchmark to design flow systems subjected to combined gradients of thermal and electric fields.

DOI: [10.1103/PhysRevFluids.9.013902](https://doi.org/10.1103/PhysRevFluids.9.013902)

I. INTRODUCTION

Thermal convection flow confined in rectangular cavities or within horizontal plates is a fundamental problem owing to its complex flow structure, and the instability features [1–4]. A classical phenomenon among thermal convection flows is the Rayleigh-Bénard convection (RBC), in which the fluid is heated from below and cooled from above. It is one of the most studied problems in the field of both fluid mechanics and heat transfer [5–9]. Various factors could influence the onset and subsequent bifurcations of Rayleigh-Bénard convection [1,4,10–13], one of which is to apply an electric field on the system [14]. The application of an electric field on the Rayleigh-Bénard convection system will induce an additional volumetric Coulomb force, which will significantly affect the flow pattern and heat transfer characteristics [15–20].

When considering the combined interactions of electric field and fluid flow [21], the subject refers to electrohydrodynamics (EHD). EHD is a topic of academic importance to researchers to understand classical physical phenomena such as electroconvection [22], ionic wind [23], and electroviscosity, etc. The free charges in a dielectric fluid medium move under the influence of the Coulomb force in the presence of an external electric field, while the movement of free charges by

*jian.wu@hit.edu.cn

the Coulomb force transfers momentum to the surrounding fluid and results in a fluid flow. This fluid flow is termed electroconvection and is analogous to the Rayleigh-Bénard convection induced by a thermal field in a planar layer of liquid. Like an RBC system, an electroconvective system is a typical nonlinear dissipative system driven by a volumetric force. However, the bifurcation phenomenon observed in these two systems is different. RBC systems typically exhibit supercritical bifurcation, i.e., when the driving parameter (Ra) exceeds the linear stability criterion, the system will smoothly shift from the state of rest to the finite-amplitude state. In contrast, an electroconvective system may exhibit sub-critical bifurcation characteristics, depending on the source of free charges. In an electroconvective system that concerns with unipolar charge injection, once the driving parameter (electric Rayleigh number T) exceeds the linear critical value [24,25], the flow strength will jump abruptly from zero to a finite value if the system is to recover back to the stationary state, the driving parameter has to decrease to another critical value (finite amplitude stability criterion [26,27]) lower than the linear stability criterion. Thus, a hysteresis loop is formed between these two criteria. Theoretical works on stability analysis of EHD instability in fluids and the relevant stability criteria are reported in the archived literature [28,29].

EHD flow motion depends on the motion of free charges due to the electric field. In a gaseous medium, free charges are mainly generated by the ionization of gas molecules. While in a liquid dielectric medium, the free charges can be generated by two mechanisms, namely (i) charge injection due to electrochemical reactions taking place at the interface of electrode and dielectric liquid (in the presence of strong electric fields) and (ii) ion conduction through dissociation-recombination mechanism (at weak or medium electric fields) [21]. Most analytical and numerical studies on electroconvective systems are based on charge injection-induced EHD flow [30]. Although charge injection-induced EHD flow exhibits strong fluid motion, the electrochemical reactions at the electrode surface lead to deterioration of the electrode surface and alters the composition of the working fluid. Thus, injection-induced EHD flow becomes unreliable for long-term applications. However, EHD conduction flow does not lead to electrode/working fluid deterioration and can function at weak/medium electric fields. EHD conduction pumping fluid flow due to ion conduction phenomenon also has several advantages, such as simple design, no moving parts, noise-free, and higher energy efficiency, which has provided a new perspective in micro-electro-mechanical systems and micro-gravity space applications [30]. EHD conduction pumping flow has attracted broad interest in recent years. The theoretical model for EHD conduction flow was first proposed by Atten *et al.* [31]. Seyed-Yagoobi *et al.* [32–34] systematically studied EHD pumping induced flow and carried out experimental works with different electrode configurations. A study on the EHD conduction pumping phenomenon with the Onsager-Wien effect was reported by Jeong *et al.* [35]. Yazdani *et al.* [36] investigated the effect of charge mobility on EHD conduction phenomenon. Recently, Vázquez *et al.* [37] has developed a mathematical model for EHD conduction pumping applicable to all sizes. Selvakumar *et al.* [38] numerically studied EHD conduction assisted natural convection in electric devices and reported that the heat transfer intensification obtained by EHD conduction pumping is more prominent at lower Rayleigh numbers and higher electric Reynolds numbers.

Establishing the stability criteria of any dynamic thermo-fluid system is essential to gain a deeper understanding and design of practical engineering systems. Concerning the stability criteria for electro-thermo-convective systems, Traoré *et al.* [14] numerically solved the whole set of the equations associated with the two 2D electro-thermo convection for the first time, obtaining the neutral stability curve in the Ra - T plane corresponding to the instability induced by heating and charge injection from the bottom plate electrode in a planar dielectric liquid layer. Wu *et al.* [39] numerically studied the influence of Prandtl number Pr and mobility parameter M on the finite amplitude convection in a parallel plate configuration. Luo *et al.* [40] developed a unified lattice Boltzmann method (LBM) for electro-thermo convection of dielectric liquids. The hysteresis loops and the sub-critical bifurcations in electro-thermo-convection of a dielectric planar liquid layer were presented. The stability diagram in the Ra - T plane for electro-thermo-convection in closed rectangular cavities was presented by Su *et al.* [41]. Recently, Peng *et al.* [42] extended the study to

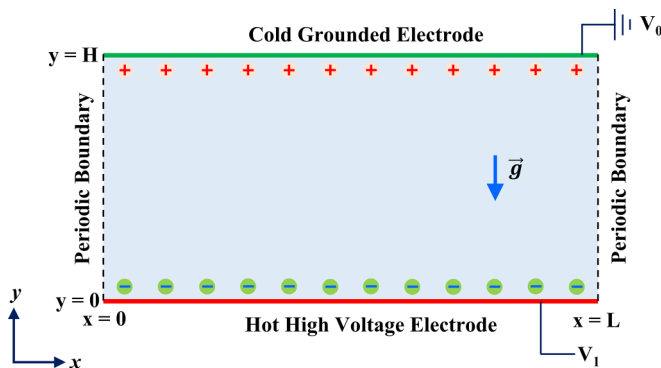


FIG. 1. Schematic representation of the computational domain.

3D electro-thermo-convection in a cubical cavity and reported the neutral stability curve and finite amplitude instability thresholds for three-dimensional electro-thermo-convection. Besides, Guan *et al.* [43] and Mordvinov *et al.* [44] studied the onset of overstable motion in electro-thermo convection when heating from above. The literature review indicates that only a few studies are reported on electro-thermo-convective instability. Furthermore, all reported studies deal with EHD flow motion due to unipolar charge injection. To the best of our knowledge, the stability criteria for combined natural convection and EHD conduction-induced electroconvection is yet to be reported in the literature. Note that, unlike unipolar injection, that is an ideal assumption for simplifying the problem with only one species of ions. At the same time, the electric conduction model is mature in weakly conducting liquids subjected to weak/medium electric field though with more types of ions. In this context, combined stability and numerical analysis of 2D electro-thermo-convection in a planar dielectric liquid layer due to the EHD conduction phenomenon (under weak/medium electric fields) is presented herein. The problem considered herein deals with RBC under the stabilizing effect caused by Onsager-Wien effect. First, hydrostatic numerical solutions for charge density distributions, electric field, and electric potential are derived. Following the solutions for the hydrostatic regime, the neutral stability curve is established by modal stability analysis. Finally, detailed numerical simulations are performed and compared with the results of stability analysis. The hysteresis loop and the associated flow and heat transfer characteristics are explained based on numerical results.

II. MATHEMATICAL FORMULATION

A. Physical description of the problem and computational domain

A horizontal planar dielectric liquid layer confined between two infinitely long parallel plate electrodes is considered, as shown in Fig. 1. The vertical gap between the plates is H , and the horizontal length of the domain is L . The bottom plate is maintained at a constant high temperature (T_1) and connected to the high electric potential (V_1). The top plate is at ambient temperature (T_0) and is grounded (V_0). The applied temperature gradient across the liquid layer will induce the gradient in permittivity, leading to dielectric force. However, under applied DC fields with space charge creation in the fluid, dielectric force is very weak compared to the Coulomb force, so dielectric force can be ignored [15,45,46]. Here, a Newtonian, incompressible dielectric liquid with mass density (ρ), kinematic viscosity (ν), and dielectric permittivity (ε) is considered. The density variation with respect to temperature is considered only in the momentum equation as per the Boussinesq approximation. All other thermophysical and dielectric properties are considered constant with variations in temperature and electric fields. In EHD conduction experiments, the residual conductivity typically falls within the range from 10^{-11} to 10^{-7} , while the applied electric

field in the system commonly reaches 10^6 (V/m) [37]. Consequently, the electric current associated with dielectric fluids is very small [21], so that the magnetic effects of the electric field are neglected. In addition, the Joule heating effect due to the electric field in dielectric fluids results in very low variation in temperature ($1 \times 10^{-4} K S^{-1}$). Thus, Joule heating effects are generally neglected in electrohydrodynamics of dielectric fluids [47].

B. Governing equations

The fully coupled numerical model for fluid flow, and heat transfer in the presence of Onsager-Wien effect includes the Navier-Stokes equations, energy equation, Poisson's equation for electric potential, and charge conservation equations for ion species [31,37].

Continuity equation:

$$\nabla \cdot \mathbf{u} = 0, \quad (1)$$

Momentum equation:

$$\rho \left(\frac{\partial \mathbf{u}}{\partial t} + \nabla \cdot (\mathbf{u}\mathbf{u}) \right) = -\nabla P + \mu \nabla^2 \mathbf{u} + (N_p - N_n) \mathbf{E} + \rho \mathbf{g} \beta (T - T_0), \quad (2)$$

Energy equation:

$$\frac{\partial T}{\partial t} + \nabla \cdot (\mathbf{u}T) = \nabla \cdot (D_T \nabla T), \quad (3)$$

where $\mathbf{u} = (u, v)$ is the fluid velocity and μ, ρ, β represent the liquid's dynamic viscosity, density, and thermal expansion coefficient, respectively. P and T stand for pressure and absolute temperature.

In the momentum equation, the third term on the right-hand side denotes the Coulomb force due to the electric field. It is to be noted that only the Coulomb force is considered in this study. As a planar dielectric fluid layer with uniform and homogeneous dielectric properties is considered, the dielectric force (a function of gradient in dielectric permittivity) becomes zero. N_p and N_n denote the charge density of positive and negative ion species, respectively. The electric field $\mathbf{E} = (E_x, E_y)$ is defined as: $\mathbf{E} = -\nabla V$, while the electric potential (V) is obtained based on the Maxwell's equations:

Poisson's equation for electric potential:

$$\nabla \cdot (\varepsilon \nabla V) = -(N_p - N_n), \quad (4)$$

where ε is the permittivity of liquid.

Two-species charge conservation equations:

$$\frac{\partial N_p}{\partial t} + \nabla \cdot J_+ = S_p, \quad (5)$$

$$\frac{\partial N_n}{\partial t} + \nabla \cdot J_- = S_n, \quad (6)$$

where the current density fluxes are given by

$$J_+ = \mathbf{u}N_p + K_+ N_p \mathbf{E} - D_+ \nabla N_p, \quad (7)$$

$$J_- = \mathbf{u}N_n - K_- N_n \mathbf{E} - D_- \nabla N_n. \quad (8)$$

Here, $K_+, K_-, D_+,$ and D_- represent the mobility and diffusion coefficient of positive and negative ion species, respectively. In the present work, the mobility and diffusion coefficient of positive ions are considered the same as the negative ions, i.e., $K_+ = K_- = K$ and $D_+ = D_- = D$ [37]. Besides, Einstein's relation is adopted, $D = K k_B T / e_0$, where k_B and e_0 are the Boltzmann constant and elementary charge. The recombination rate k_R is determined by Langevin's formula as $k_R = (K_+ + K_-) / \varepsilon = 2K / \varepsilon$ [48]. S_p and S_n are the source terms contributed by the generation and

disappearance of ions, while the only source of ions is the dissociation-recombination processes of the weak electrolytes in bulk, which is a reversible process governed by dissociation rates (k_D) and recombination rates (k_R):



when the fluid is under equilibrium, we have

$$k_D c_0 = k_R N_p^{\text{eq}} N_n^{\text{eq}} = k_R (N_{\text{eq}})^2. \quad (10)$$

AB is a simple neutral electrolyte species that can produce positive ions (A^+) and negative ions (B^-) through the reversible process. c_0 represents the concentration of neutral molecules. The superscript 'eq' means the value in equilibrium. Especially, owing to the electro-neutrality of the solution, $N_p^{\text{eq}} = N_n^{\text{eq}} = N_{\text{eq}}$. The source terms can be written as follows:

$$S_p = k_D c - k_R N_p N_n, \quad (11)$$

$$S_n = k_D c - k_R N_p N_n. \quad (12)$$

According to the model proposed by Onsager, the formula for field-enhanced dissociation is given as

$$k_D(|\mathbf{E}|) = F[w(|\mathbf{E}|)] k_{D0} = \frac{I_1[4w(|\mathbf{E}|)]}{2w(|\mathbf{E}|)} k_{D0}. \quad (13)$$

In Eq. (13), the Onsager function $F = I_1[4w(|\mathbf{E}|)]/2w(|\mathbf{E}|)$ and the enhanced dissociation rate coefficient $w(|\mathbf{E}|) = L_B/L_O = (\frac{e^3 |\mathbf{E}|}{16\pi \epsilon k_B^2 T^2})^{1/2}$, where $L_B = e_0^2/8\pi \epsilon k_B T$ is Bjerrum distance and $L_O = \sqrt{e_0/4\pi \epsilon |\mathbf{E}|}$ is Onsager distance. Here, $(e^3/16\pi \epsilon k_B^2 T^2)^{1/2}$ is defined as γ , and the function $I_1()$ is the modified Bessel function:

$$I_1(x) = \sum_{k=0}^{\infty} \frac{(x/2)^{1+2k}}{k!(k+1)!}. \quad (14)$$

Therefore, the Onsager function can be expressed as

$$F[w(|\mathbf{E}|)] = \sum_{k=0}^{\infty} \frac{(4\gamma |\mathbf{E}|)^k}{k!(k+1)!} = 1 + 2\gamma |\mathbf{E}| + \frac{4}{3}\gamma^2 |\mathbf{E}|^2 + \dots \quad (15)$$

Present study considers only the first two terms, i.e., $(F[w(|\mathbf{E}|)] = 1 + 2\gamma |\mathbf{E}|)$ [49]. The resultant ion transport equations for positive and negative ions are as follows:

$$\frac{\partial N_p}{\partial t} + \nabla \cdot \mathbf{J}_+ = k_R (N_{\text{eq}}^2 F[w(|\mathbf{E}|)] - N_p N_n), \quad (16)$$

$$\frac{\partial N_n}{\partial t} + \nabla \cdot \mathbf{J}_- = k_R (N_{\text{eq}}^2 F[w(|\mathbf{E}|)] - N_p N_n). \quad (17)$$

Above set of governing equations are rendered in nondimensional form based on the following characteristic scalings:

$$\begin{aligned} x^* &= \frac{x}{H}; & y^* &= \frac{y}{H}; & t^* &= \frac{tK(V_1 - V_0)}{H^2}; \\ \mathbf{u}^* &= \frac{\mathbf{u}H}{K(V_1 - V_0)}; & V^* &= \frac{V - V_0}{V_1 - V_0}; & \mathbf{E}^* &= \frac{\mathbf{E}H}{V_1 - V_0}; \\ \theta^* &= \frac{\theta - \theta_0}{\theta_1 - \theta_0}; & P^* &= \frac{PH^2}{\rho K^2 (V_1 - V_0)^2}. \end{aligned} \quad (18)$$

TABLE I. Summary of nondimensional boundary conditions used in this study.

| Location | Velocity (\mathbf{u}) | Temperature (θ) | Electric potential (V) | Charge density (N_p, N_n) |
|---|---|---|---|---|
| Bottom wall ($\mathbf{y} = \mathbf{0}$) | $\mathbf{u} = \mathbf{0}$ | $\theta_l = 1$ | $V_l = 1$ | $\frac{\partial N_n}{\partial y} = 0; N_p = 0$ |
| Top wall ($\mathbf{y} = \mathbf{L}$) | $\mathbf{u} = \mathbf{0}$ | $\theta_r = 0$ | $V_r = 0$ | $\frac{\partial N_p}{\partial y} = 0; N_n = 0$ |
| Lateral walls ^a | $[\frac{\partial \mathbf{u}}{\partial x}]_l = [\frac{\partial \mathbf{u}}{\partial x}]_r$ | $[\frac{\partial \theta}{\partial x}]_l = [\frac{\partial \theta}{\partial x}]_r$ | $[\frac{\partial V}{\partial x}]_l = [\frac{\partial V}{\partial x}]_r$ | $[\frac{\partial N_{p,n}}{\partial x}]_l = [\frac{\partial N_{p,n}}{\partial x}]_r$ |

^aThe subscripts l and r denote the values at left and right boundaries, respectively.

The resultant dimensionless governing equations are as follows:

$$\nabla \cdot \mathbf{u} = 0, \quad (19)$$

$$\nabla \cdot (\nabla V) = -C_0(N_p - N_n), \quad (20)$$

$$\mathbf{E} = -\nabla V, \quad (21)$$

$$\frac{\partial \mathbf{u}}{\partial t} + \nabla \cdot (\mathbf{u}\mathbf{u}) = -\nabla p + \frac{1}{\text{Re}_E} \nabla^2 \mathbf{u} + M^2 C_0 (N_p - N_n) \mathbf{E} + \frac{\text{Ra}}{\text{Pr}(\text{Re}_E)^2} \theta \mathbf{e}_y, \quad (22)$$

$$\frac{\partial N_p}{\partial t} + \nabla \cdot [N_p \cdot (\mathbf{u} + \mathbf{E})] - \alpha \nabla^2 N_p = 2C_0 [F[w(|\mathbf{E}|)] - N_p N_n], \quad (23)$$

$$\frac{\partial N_n}{\partial t} + \nabla \cdot [N_n \cdot (\mathbf{u} - \mathbf{E})] - \alpha \nabla^2 N_n = 2C_0 [F[w(|\mathbf{E}|)] - N_p N_n], \quad (24)$$

$$\frac{\partial \theta}{\partial t} + \nabla \cdot (\mathbf{u}\theta) = \frac{1}{\text{PrRe}_E} \nabla^2 \theta. \quad (25)$$

The * symbol representing the nondimensional variables is neglected for the purpose of simplicity. Following dimensionless parameters arise as a result of the nondimensionalization.

$$\begin{aligned} \text{Re}_E &= \frac{\rho K (V_1 - V_0)}{\mu}; & \text{Pr} &= \frac{\mu}{\rho D_T}; & \text{Ra} &= \frac{\rho g \beta H^3 \Delta T}{\mu D_T}; \\ M &= \frac{1}{K} \sqrt{\frac{\varepsilon}{\rho}}; & \alpha &= \frac{D}{K (V_1 - V_0)}; & C_0 &= \frac{N_{\text{eq}} H^2}{\varepsilon (V_1 - V_0)}. \end{aligned} \quad (26)$$

The conduction number (C_0) is a key parameter to differentiate the regimes in EHD conduction: ohmic and saturation. It represents the ratio of ionic transit time ($H^2/[K(V_1 - V_0)]$) and relaxation time (ε/σ_0), where $\sigma_0 = 2KN_{\text{eq}}$ is residual conductivity. Rayleigh number (Ra) is the ratio of buoyancy force to viscous force, representing the strength of buoyancy driving force. The Prandtl number (Pr) represents the ratio of momentum diffusivity to thermal diffusivity. In contrast, the hydrodynamic to ionic mobility ratio is represented by the ionic mobility parameter (M), which both depend on fluid properties. α is the nondimensional ionic diffusion coefficient, and the electric Reynolds number (Re_E) indicates the dimensionless applied electric field.

C. Boundary and initial conditions

A summary of dimensionless boundary conditions used in this study is presented in Table I. Both the plate electrodes are infinitely long in the x direction, impermeable, electrically and thermally perfectly conductors. The no-slip boundary condition is applied over both the horizontal plate electrodes. As the electrodes are infinitely long, the periodic boundary condition is considered for all the variables along the lateral walls of the domain. The bottom and top plates are hot and cold walls, respectively. Likewise, a high electric potential is applied over the bottom wall, and the top wall is grounded. Neumann boundary for negative ions and Dirichlet boundary condition for

positive ions are applied over the bottom wall. Neumann boundary for positive ions and Dirichlet boundary condition for negative ions are applied over the top wall. Therefore, the positive and negative charges migrate and accumulate near the top and bottom electrodes, respectively. The accumulation of charges near the oppositely charged electrodes is termed the heterocharge layers, as shown in Fig. 1. As for initial conditions, there are two situations in this study: (i) initiate the simulation with zero-field values set for all variables and (ii) initialize the simulations with the convective state that is obtained previously.

III. SOLUTION METHODOLOGY

A. Numerical simulations

The mathematical model for RBC under the influence of Onsager-Wien effect are solved using OpenFOAM's finite-volume method (FVM)-based framework. The governing equations for electric potential and two-species charge conservation equations are incorporated into the existing solver for fluid flow and heat transfer in OpenFOAM. All the simulations performed here are transient, and standard finite-volume procedures for discretization available in OpenFOAM are utilized [50]. The temporal derivatives in the governing equations are discretized with a backward scheme. The linear scheme is used to discretize the gradient terms. The convection term in the momentum equation is discretized using the (Quadratic Upwind Interpolation for Convective Kinetics) QUICK scheme [51], while a total variation diminishing (TVD) Van Leer scheme [52] is used for the discretization of the convection and electro-migration terms in charge transport equations. For more details, please refer to Ref. [53].

B. Stability analysis

The linear stability of the hydrostatic state is studied in this work. The standard method of small perturbations is adopted to determine the onset value of the system. When small perturbations are applied to the hydrostatic state of the system, if the perturbations grow with time, then the system is unstable. In contrast, if the perturbations decay, then the system is stable. The critical Rayleigh numbers Ra_c represent the driving parameter's smallest value, triggering the growth of perturbations in time. There are several nondimensional parameters to control the system. The other nondimensional parameters need to be fixed to determine the critical driving parameter Ra_c . This work calculates Pr and M based on the property of a common dielectric fluid used as a working fluid in EHD applications. Several conduction numbers C_0 are chosen, then the critical Rayleigh numbers Ra_c corresponding to each conduction number C_0 are identified. In the present work, the buoyancy force measured with Ra plays a destabilizing role in the system, and conduction number C_0 is a key nondimensional parameter in conduction; thus, this work focuses on the effect of C_0 on the Ra_c .

IV. RESULTS AND DISCUSSION

This study considers Rayleigh-Bénard convection with electric field induced Onsager-Wien effect in a planar dielectric liquid layer confined between two infinitely long parallel plate electrodes. The Onsager-Wien effect considered here is due to the electric field enhanced dissociation of ions taking place at weak/medium electric fields. This is a combination of classical RBC and stabilizing effect induced by the Onsager-Wien effect. An extensive parametric study is presented using both Rayleigh number (Ra) and conduction number (C_0) as control parameters. The nondimensional parameters denoting the working fluid's properties are Prandtl number (Pr) and mobility parameter (M). In the present study, Pr and M are chosen as 157.1 and 54.1, respectively, corresponding to the properties of transformer oil (refer to Table II). The value of Re_E has been established at 2.65 based on the parameter set used in our simulations. The results of stability and numerical analyses are presented in this section. The system's behavior in hydrostatic and electrohydrodynamic equilibrium states is presented in Sec. IV A. Then, the discussions on stability analysis and the neutral stability

TABLE II. Thermophysical and dielectric properties of transformer oil [54–56].

| Property | Value |
|--|-------------------------|
| Density ρ (kgm ⁻³) | 895.5 |
| Dynamic viscosity μ (PaS) | 0.011 |
| Thermal conductivity η (Wm ⁻¹ K ⁻¹) | 0.13 |
| Thermal expansion coefficient β (K ⁻¹) | 0.0007 |
| Dielectric permittivity ε (Fm ⁻¹) | 18.41×10^{-12} |
| Ionic mobility K (m ² s ⁻¹ V ⁻¹) | 2.65×10^{-09} |
| Electric conductivity σ (Sm ⁻¹) | 1.20×10^{-12} |

curve are provided in Sec. IV B. Finally, Secs. IV C and IV D discuss the flow and heat transfer characteristics.

A. Hydrostatic and electrohydrodynamic equilibrium state

For the configuration considered herein, the Coulomb force, due to the electric field, stabilizes the system, and the buoyancy force strives to destabilize the system. When the Rayleigh number Ra is below a critical value, the system has a stable state with no fluid motion. At this state, the buoyancy force is weak to overcome the stabilizing effect of the electric forces and the viscous dissipation. Therefore, the system remains in the state of rest, which is termed hydrostatic and electrohydrodynamic equilibrium state. Once the parameter (Ra) is raised above the critical value (Ra_c), the buoyancy forces become strong enough to destabilize the system, and the fluid motion is observed. This state is referred to as the electrohydrodynamic state. In an electrohydrodynamic state, the electric, flow, and thermal fields are closely coupled. The two body forces drive the flow field, and the flow influences the body forces through thermal and electric charge transport. This strong nonlinear coupling between the three fields results in a complex fluid motion.

The solutions to Eqs. (19) ~ (25) when the system is in hydrostatic (no fluid motion) are derived in this section. Owing to the periodic boundary conditions considered in the x direction and the hydrostatic state, the expressions of physical variables are only a function of y coordinates. Thus, $N_{p0} = N_{p0}(y)$, $N_{n0} = N_{n0}(y)$, $V_0 = V_0(y)$, $E_0 = E_0(y)$, $\theta_0 = \theta_0(y)$. By imposing $\mathbf{u} = 0$ and $\partial_t = 0$, the equations for the hydrostatic state are

$$\nabla \cdot (N_{p0} \mathbf{E}_0) - \alpha \nabla^2 N_{p0} = 2Co(1 + 2\gamma E_0 - N_{p0}N_{n0}), \quad (27)$$

$$-\nabla \cdot (N_{n0} \mathbf{E}_0) - \alpha \nabla^2 N_{n0} = 2Co(1 + 2\gamma E_0 - N_{p0}N_{n0}), \quad (28)$$

$$\mathbf{E}_0 = -\nabla V_0, \quad (29)$$

$$\nabla^2 V_0 = Co(N_{p0} - N_{n0}), \quad (30)$$

$$\nabla^2 \theta_0 = 0. \quad (31)$$

The boundary conditions associated with these equations are shown in Table I. In a hydrostatic state, there is no fluid velocity; thus, the temperature field is decoupled from other variables. Thus, the temperature profile takes the following form in y direction:

$$\theta_0 = 1 - y \quad (0 < y < 1). \quad (32)$$

The analytical solutions for variables pertaining to electrostatic Eqs. (27) ~ (30) cannot be directly obtained, owing to the complexity of equations. Newton's method is introduced here to acquire approximate solutions of Eqs. (27) ~ (30) [57]. Newton's method is a way to quickly find a good approximation for the root of a real-valued function. It uses the idea that a continuous and

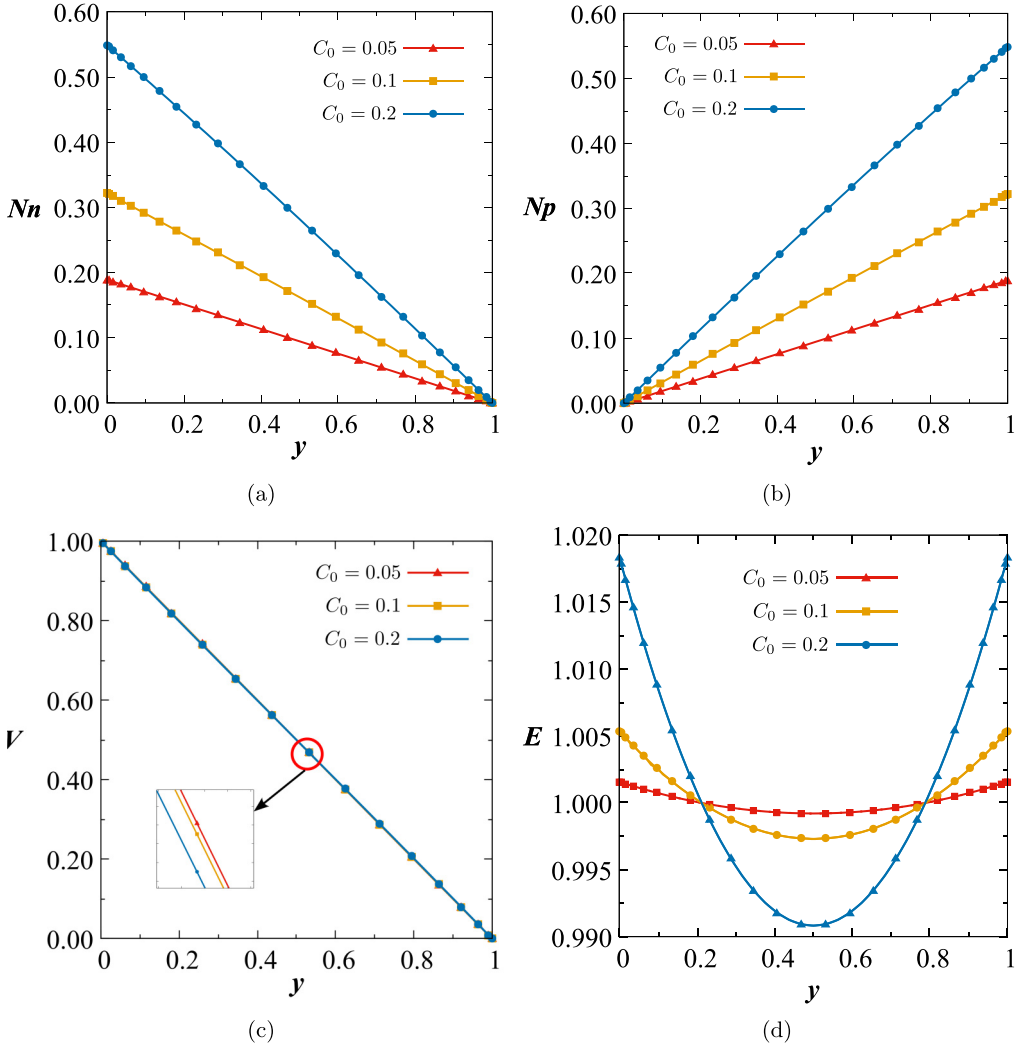


FIG. 2. Variation of the physical quantities in the hydrostatic state. (a) Positive-charge density (N_p), (b) negative-charge density (N_n), (c) electric potential (V), and (d) electric field (\mathbf{E}). Lines represent results from Newton's method and symbols represent FVM results from OpenFOAM.

differentiable function can be approximated by a straight-line tangent. The distributions of physical variables N_p , N_n , V , and \mathbf{E} in the y direction obtained by the Newton's method are presented in Figs. 2(a) ~ 2(d). The FVM-based numerical solution performed in OpenFOAM to Eqs. (27) ~ (30) gives the distribution of physical variables (positive-charge density N_p , negative-charge density N_n , electric potential V , and electric field \mathbf{E}) in the computational domain (see Fig. 3). The heterocharge layer formation is noticed in Figs. 3(a) and 3(b). For $C_0 = 0.1$, the system is in a saturation regime. Thus, the heterocharge layers are very thick. The electric potential varies linearly in y direction from the highest value ($V = 1$) near the bottom high-voltage electrode to the lowest value ($V = 0$) at the top grounded electrode. The electric field distribution is shown in Fig. 3(c). The electric field intensity is relatively strong near the electrodes and lowest in the center of the domain. The distribution of physical variables obtained by FVM simulations and Newton's method perfectly match each other (Fig. 2).

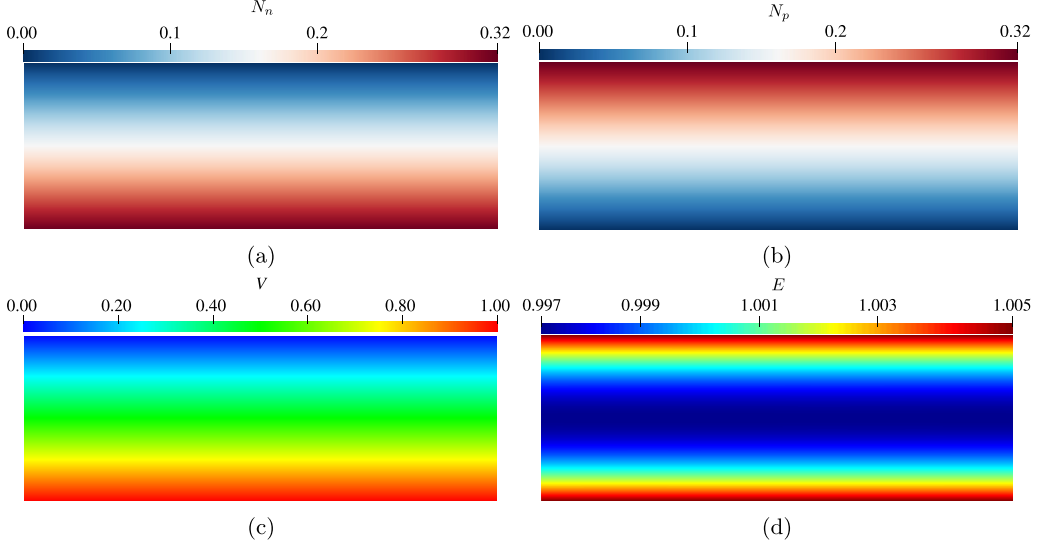


FIG. 3. Distribution of physical variables in hydrostatic state (obtained by numerical simulations). (a) Negative-charge distribution (N_n), (b) positive-charge distribution (N_p), (c) electric potential (V), and (d) electric field (\mathbf{E}) for $C_0 = 0.1$.

B. Modal stability analysis

According to linear stability theory, the variables in the system can be decomposed as the sum of base state and perturbation:

$$N_p(x, y, t) = N_{p0}(y) + N'_p(x, y, t), \quad (33)$$

$$N_n(x, y, t) = N_{n0}(y) + N'_n(x, y, t), \quad (34)$$

$$V(x, y, t) = V_0(y) + V'(x, y, t), \quad (35)$$

$$\mathbf{E}(x, y, t) = \mathbf{E}_0(y) + \mathbf{E}'(x, y, t), \quad (36)$$

$$\theta(x, y, t) = \theta_0(y) + \theta'(x, y, t), \quad (37)$$

$$p(x, y, t) = p_0(y) + p'(x, y, t), \quad (38)$$

$$\mathbf{u}(x, y, t) = \mathbf{u}'(x, y, t). \quad (39)$$

Here, $\mathbf{u}' = (u', v')$. The perturbation quantities are assumed to be much smaller than the basic state quantities. By substituting the decompositions into dimensionless equations and ignoring the higher-order terms in the perturbations, the stability equations read

$$\nabla \cdot \mathbf{u}' = 0, \quad (40)$$

$$\nabla^2 V' + Co(N'_p - N'_n) = 0, \quad (41)$$

$$\frac{\partial u'}{\partial t} = -\frac{1}{\text{Re}_E^2} \frac{\partial p'}{\partial x} + \frac{1}{\text{Re}_E} \nabla^2 u' + M^2 Co \left[(N_{p0} - N_{n0}) \left(-\frac{V'}{\partial x} \right) \right], \quad (42)$$

$$\frac{\partial v'}{\partial t} = -\frac{1}{\text{Re}_E^2} \frac{\partial p'}{\partial y} + \frac{1}{\text{Re}_E} \nabla^2 v' + \frac{\text{Ra}}{\text{PrRe}_E^2} \theta' + M^2 Co \left[(N_{p0} - N_{n0}) \left(-\frac{V'}{\partial y} \right) + (N'_p - N'_n) \mathbf{E}_0 \right], \quad (43)$$

$$\begin{aligned} \frac{\partial N'_p}{\partial t} + \frac{\partial N_{p0}}{\partial y} \left(v - \frac{\partial V'}{\partial y} \right) - N_{p0} \nabla^2 V' + \frac{\partial E_0}{\partial y} N'_p + E_0 \frac{\partial N'_p}{\partial y} - \alpha \nabla^2 N'_p + 2Co(N_{p0} N'_n + N'_p N_{n0}) \\ - 2Co[2\gamma(|\mathbf{E}_0 + \mathbf{E}'| - |\mathbf{E}_0|)] = 0, \end{aligned} \quad (44)$$

$$\begin{aligned} \frac{\partial N'_n}{\partial t} + \frac{\partial N_{n0}}{\partial y} \left(v + \frac{\partial V'}{\partial y} \right) + N_{n0} \nabla^2 V' - \frac{\partial E_0}{\partial y} N'_n - E_0 \frac{\partial N'_n}{\partial y} - \alpha \nabla^2 N'_n + 2Co(N_{p0} N'_n + N'_p N_{n0}) \\ - 2Co[2\gamma(|\mathbf{E}_0 + \mathbf{E}'| - |\mathbf{E}_0|)] = 0, \end{aligned} \quad (45)$$

$$\frac{\partial \theta'}{\partial t} - v = \frac{1}{\text{PrRe}_E} \nabla^2 \theta'. \quad (46)$$

The standard way to proceed is to write the primed equations as a product of an exponential function depending on time and a function depending on the spatial variables alone:

$$\mathbf{u}' = \mathbf{u}'(z) \exp(\sigma t) \exp(ikx), \quad (47)$$

$$V' = V'(y) \exp(\sigma t) \exp(ikx), \quad (48)$$

$$N'_p = N'_p(y) \exp(\sigma t) \exp(ikx), \quad (49)$$

$$N'_n = N'_n(y) \exp(\sigma t) \exp(ikx), \quad (50)$$

$$\theta' = \theta'(y) \exp(\sigma t) \exp(ikx). \quad (51)$$

Here, k denotes wave number, while σ represents the growth rate. If $\sigma > 0$, then the perturbations increase with time, which means the system is unstable, while if $\sigma < 0$, then the perturbations decrease with time, which means the system is stable. Therefore, the onset of the system corresponds to the situation with $\sigma = 0$. Besides, a common practice in stability analysis to eliminate the pressure term is $\partial/\partial x$ [$\partial/\partial y$ (42)– $\partial/\partial x$ (43)]. If introducing Eqs. (47) ~ (51) into Eqs. (40) ~ (46) and dropping ', then the equations become

$$\nabla^2 V + Co(N_p - N_n) = 0, \quad (52)$$

$$\begin{aligned} \sigma(-\nabla^2 v) = \frac{1}{\text{Re}_E} \nabla^2(-\nabla^2 v) - \frac{\text{Ra}}{\text{PrRe}_E^2} \frac{\partial^2 \theta}{\partial x^2} + M^2 Co \left[\frac{\partial(N_{p0} - N_{n0})}{\partial y} \left(-\frac{\partial^2 V}{\partial x^2} \right) \right. \\ \left. - |\mathbf{E}_0| \frac{\partial^2(N_p - N_n)}{\partial x^2} \right], \end{aligned} \quad (53)$$

$$\begin{aligned} -\sigma N_p = \frac{\partial N_{p0}}{\partial y} \left(v - \frac{\partial V}{\partial y} \right) - N_{p0} \nabla^2 V + 4\gamma Co \frac{\partial V}{\partial y} + \frac{\partial E_0}{\partial y} N_p + E_0 \frac{\partial N_p}{\partial y} - \alpha \nabla^2 N_p \\ + 2Co(N_{p0} N_n + N_p N_{n0}), \end{aligned} \quad (54)$$

$$\begin{aligned} -\sigma N_n = \frac{\partial N_{n0}}{\partial y} \left(v + \frac{\partial V}{\partial y} \right) + N_{n0} \nabla^2 V + 4\gamma Co \frac{\partial V}{\partial y} - \frac{\partial E_0}{\partial y} N_n - E_0 \frac{\partial N_n}{\partial y} - \alpha \nabla^2 N_n \\ + 2Co(N_{p0} N_n + N_p N_{n0}), \end{aligned} \quad (55)$$

$$\sigma \theta = v + \frac{1}{\text{PrRe}_E} \nabla^2 \theta, \quad (56)$$

with the boundary conditions for the fluctuations:

$$\begin{aligned}
 y = 0 : v = 0; \quad V = 0; \quad N_p = 0; \quad \frac{\partial N_n}{\partial y} = 0; \quad \theta = 0; \\
 y = 1 : v = 0; \quad V = 0; \quad \frac{\partial N_p}{\partial y} = 0; \quad N_n = 0; \quad \theta = 0.
 \end{aligned} \tag{57}$$

Equations (52) ~ (56) with boundary conditions (57) define an eigenvalue problem. To solve the eigenvalue problem, the spectral method is introduced based on collocation points chosen as the roots of Chebyshev polynomials [58]. The linear equations could be expressed by

$$L(\sigma, \text{Ra}, k) = 0. \tag{58}$$

Octave [60] is a powerful open-source platform used to solve the differential equations. We tested several N of collocation points to obtain convergent results, and a sufficient number N is chosen as Chebyshev grids. To acquire the whole solution, we traversed the entire parameter domain (Ra , k) to gain the value of σ , that is, $\sigma = G(\text{Ra}, k)$, then we use the plane $\sigma = 0$ to intercept the function $\sigma = G(\text{Ra}, k)$. The intersection of the plane and the function $\sigma = G(\text{Ra}, k)$ is the stability curve, as shown in Fig. 4. The critical Rayleigh numbers Ra_c for different conduction numbers C_0 represented by yellow points are summarized in Fig. 5. Figure 5 also shows the neutral stability curve predicted by the reference corresponds to the case of $C = L = N = 0$ [59], depicted by the green line. It is worth noting that a key distinction between the problem under consideration here and the work of Pontiga et al. is that they ignored the field-enhanced dissociation effect, causing the difference between our results and the onset value predicted by the reference. Due to the field-enhanced dissociation effect, there will be an increase in charge density. This, in turn, will result in a stronger electric force, leading to a higher Ra_c . To assess the accuracy of modal stability analysis, it is performed on the same governing equations as Ref. [59] and the resulting onset values are indicated by triangles in Fig. 5, which exhibits good agreement with Ref. [59] with maximum relative error of 2.8%. Besides, the critical Rayleigh number Ra_c is also calculated from numerical simulations. A simulation with a high value of Ra is first performed to reach a steady state. The obtained steady state solution is the initial condition for the next simulation with a lower value of Ra . This procedure is repeated with Ra decreasing in steps of 50 until the flow motion stops, and we define the previous value of Ra with the fluid flow as Ra_c . The comparison of the critical Rayleigh numbers Ra_c obtained by modal stability analysis and FVM numerical simulations are presented in Table III. The results of the stability analysis and the FVM simulations agree with each other.

C. Flow features of electro-thermo-convection

With the establishment of critical Rayleigh number Ra_c in Sec. IV B, numerical simulations are performed at low and moderate values of Rayleigh number ($1 \times 10^3 \leq \text{Ra} \leq 50 \times 10^3$ and at conduction numbers $C_0 = 0.05, 0.1$ and 0.2). It is noted that Ra and C_0 vary by varying the temperature difference and the vertical gap H between the electrodes. The horizontal length of the domain is fixed as $L = (2\pi H)/k_c$ (k_c being the critical wave number).

Figures 6(a) ~ 6(c) present the variation of the maximum velocity $U_{\max} = \|\mathbf{u}\|_2$ in the domain with respect to Ra at $C_0 = 0.05, 0.1$, and 0.2 , respectively. In the numerical cases, two different initial conditions are considered, the one is initialized with the zero fields, while the other starts with the convective state that is obtained previously. The upward arrows signify cases that begin with the convective state corresponding to lower Ra , while the downward arrows correspond to the cases that commence with the convective state with higher Ra . It is to be noted that all the results presented herein correspond to the steady state values of the transient simulations. In general, U_{\max} values grow with the increase of Ra . In Fig. 6, the points marked with red color can be obtained by initializing the simulations by zero-field values or the solutions from the previous convective states. In contrast, the yellow colored points can only be obtained by simulations initialized with solution from the preceding convective state. For $C_0 = 0.05$ and 0.1 , we observe two solution branches, S_1 (upper

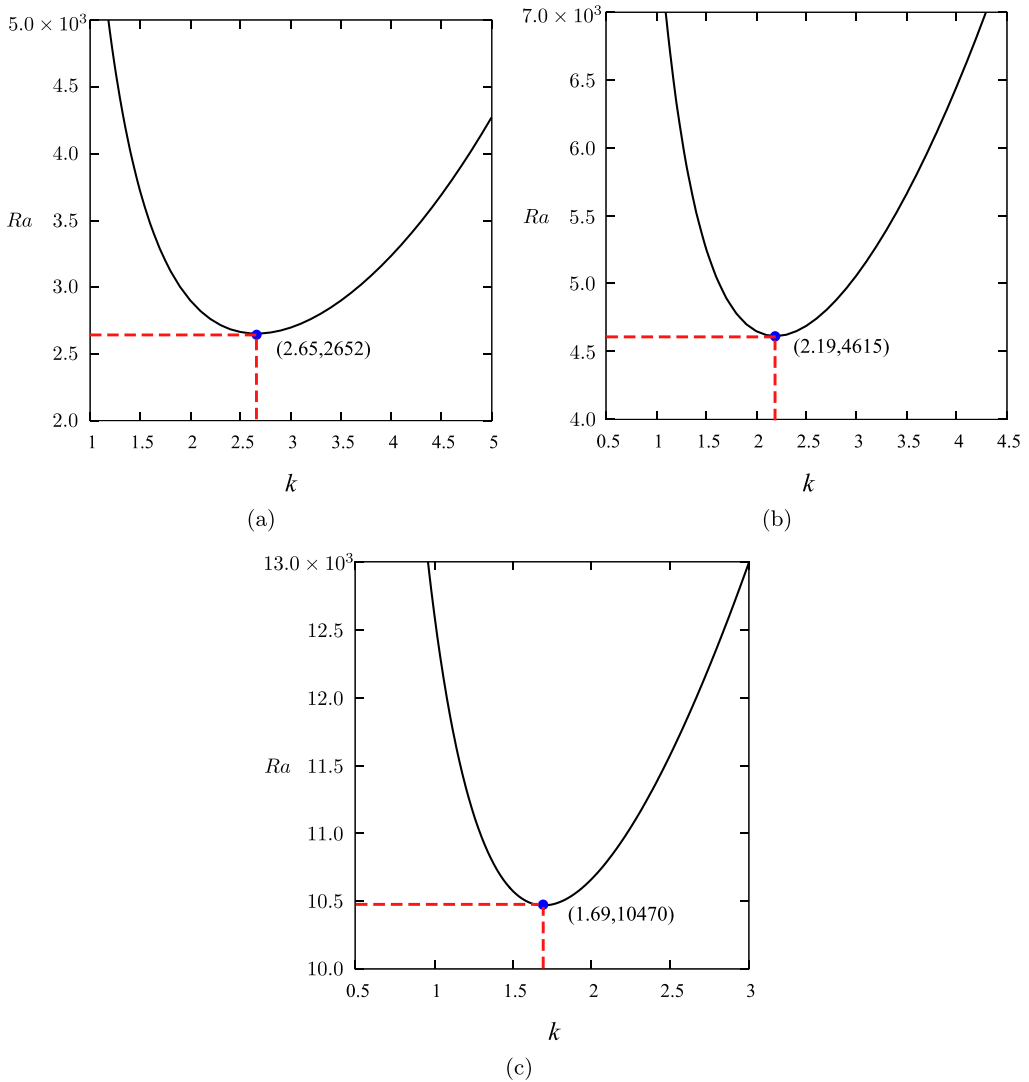


FIG. 4. Variation of critical Rayleigh number (Ra_c) with respect to wave number (k) at different values of conduction number (a) $C_0 = 0.05$, (b) $C_0 = 0.1$, and (c) $C_0 = 0.2$.

branch) and S_2 (lower branch). The critical Rayleigh number Ra_c values obtained by the modal stability analysis corresponding to $C_0 = 0.05$, 0.1 , and 0.2 are 2652, 4615, and 10470, respectively. It is to be understood that the symmetric equal electrodes considered in this configuration lead to stabilization or restriction of the fluid motion [61]. With the increase of C_0 , the stabilization effect of the electric field is stronger. Thus, higher values of Ra_c are required at higher values of C_0 . Dual solutions exist for $C_0 = 0.05$ and 0.1 , i.e., the same combinations of control parameters Ra and C_0 can lead to different flow patterns depending on the initial conditions. In Figs. 6(a) and 6(b), the upper branches (S_1) marked with solid lines are characterized by a flow structure with single pair of vortices. However, the lower solution branch (S_2) marked with dotted lines exhibits a flow structure with two pairs of vortices. The critical value of Ra at which the flow pattern shifts from single-vortex pair to double-vortex pairs, while Ra decreases, is referred to as Ra_{s1} . Likewise, Ra_{s2}

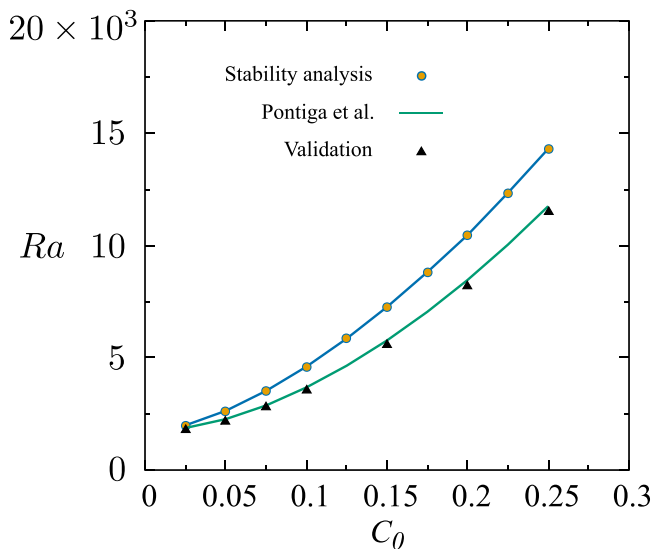


FIG. 5. Variation of critical Rayleigh number (Ra_c) as a function of conduction number (C_0). Circles denote the onset value for current study obtained by the stability analysis, green line is from Ref. [59], and the triangles denote the onset value obtained by stability analysis for the problem considered in Ref. [59].

marks the shift in flow pattern when Ra increases. In Figs. 6(a) and 6(b), when Ra approaches Ra_{s1} or Ra_{s2} , the simulations are done in steps of $\Delta Ra = 10$. For instance, at $C_0 = 0.05$, the shift in flow patterns occurs when Ra increases from 48 020 to 48 030 and 8350 to 8340. Therefore, Ra_{s1} and Ra_{s2} values for $C_0 = 0.05$ correspond to 8350 and 48 020, respectively. Synonymous with $C_0 = 0.05$, $C_0 = 0.1$ exhibits two solution branches. However, two flow patterns are observed in the lower solution branch. In S_2 at $C_0 = 0.1$, the lower values of Ra correspond to a flow structure with two pairs of symmetric vortices. Whereas, at higher values of Ra , the double-pair vortex structures are not perfectly symmetric. The Ra_{s1} and Ra_{s2} values corresponding to $C_0 = 0.1$ are 10 760 and 43 520, respectively. Overall, the red and yellow dots are determined by the choice of initial conditions for the simulations. The occurrence of solution branch S_1 and S_2 is jointly determined by the value of the control parameters and the initial conditions. The values of Ra_{s1} and Ra_{s2} are determined by the increase or decrease of Ra . Unlike the cases of $C_0 = 0.05$ and 0.1, the case with $C_0 = 0.2$ requires a much higher value Ra_c to overcome the stabilization effect of electric field and to initiate the fluid motion. Only one solution branch exists at $C_0 = 0.2$, and the value of U_{max} increases with an increase in Ra . Close to $Ra \geq 22\,000$, the flow loses its steady-state behavior and enters an unsteady regime.

Flow patterns and velocity fields corresponding to solution branches S_1 and S_2 observed at $0.05 \leq C_0 \leq 0.2$ and $12 \times 10^3 \leq Ra \leq 50 \times 10^3$ are presented in Fig. 7. Irrespective of the values of C_0 and the solution branches, the flow intensity (velocity magnitude) is directly proportional to Ra . For $C_0 = 0.05$, the solution branch S_1 is characterized by a flow structure with two perfectly

TABLE III. Comparison of onset value Ra_c predicted by modal stability analysis and numerical simulations.

| C_0 | 0.05 | 0.1 | 0.2 |
|--------------------------|-------------|-------------|-----------------|
| Modal stability analysis | 2652 | 4615 | 10 470 |
| Numerical simulation | 2600 ~ 2650 | 4550 ~ 4600 | 10 300 ~ 10 350 |
| Maximum relative error | 1.96% | 1.41% | 1.62% |

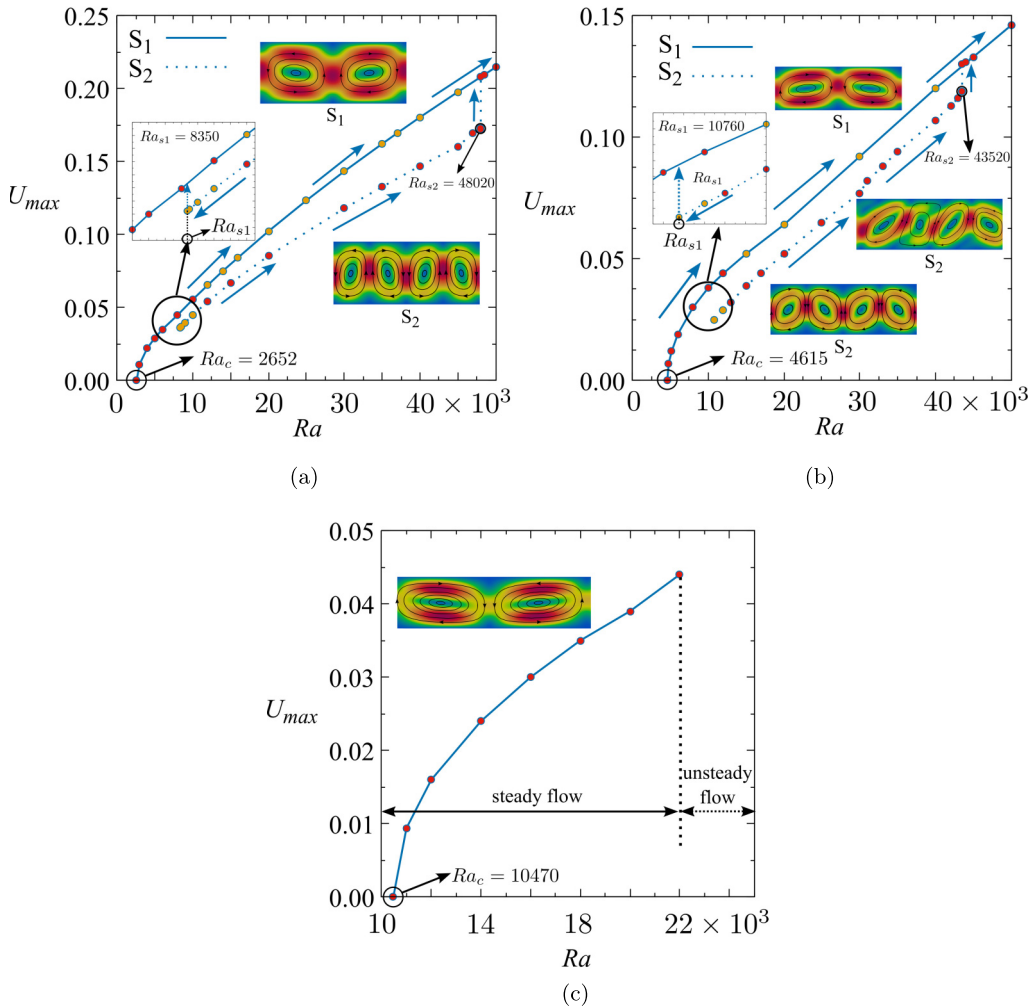


FIG. 6. Variation of the maximum velocity U_{max} as a function of Rayleigh number (Ra) at different conduction numbers (a) $C_0 = 0.05$, (b) $C_0 = 0.1$, and (c) $C_0 = 0.2$. (S_1 and S_2 represent the flow pattern of a pair of vortices and two pairs of vortices, respectively.)

symmetric vortices. In S_2 , a shift from a bicellular flow (single pair of vortices) structure to flow with four cells (two pairs of vortices) is noted. Both in S_1 and S_2 , the maximum velocity distribution is always found in the region between two vortices. At $C_0 = 0.1$, S_1 is characterized by a bicellular flow structure with two symmetric vortices. The vortex shapes observed at lower values of Ra favor the maximum velocity distribution in the proximity of electrodes, which is due to the more symmetrical cell. Whereas, at higher values of Ra the peak velocity distribution is noted in between the vortices. Same as $C_0 = 0.05$, the S_2 branch of $C_0 = 0.1$ also shifts from a bicellular flow structure to a flow pattern with four cells. In S_2 , the vortex structures favor the peak velocity distributions in between the vortices. In $C_0 = 0.2$, there exists only one solution branch. With increasing Ra , the flow gets stronger. The flow structure is mainly bicellular. However, it is to be noted that the velocity distributions are weaker by one order of magnitude as compared to $C_0 = 0.05$ and 0.1 . The stabilization effect of the electric field due to the symmetric electrodes restricts the fluid motion. The regions of high velocity distributions are noted near the electrodes. One peculiar observation is

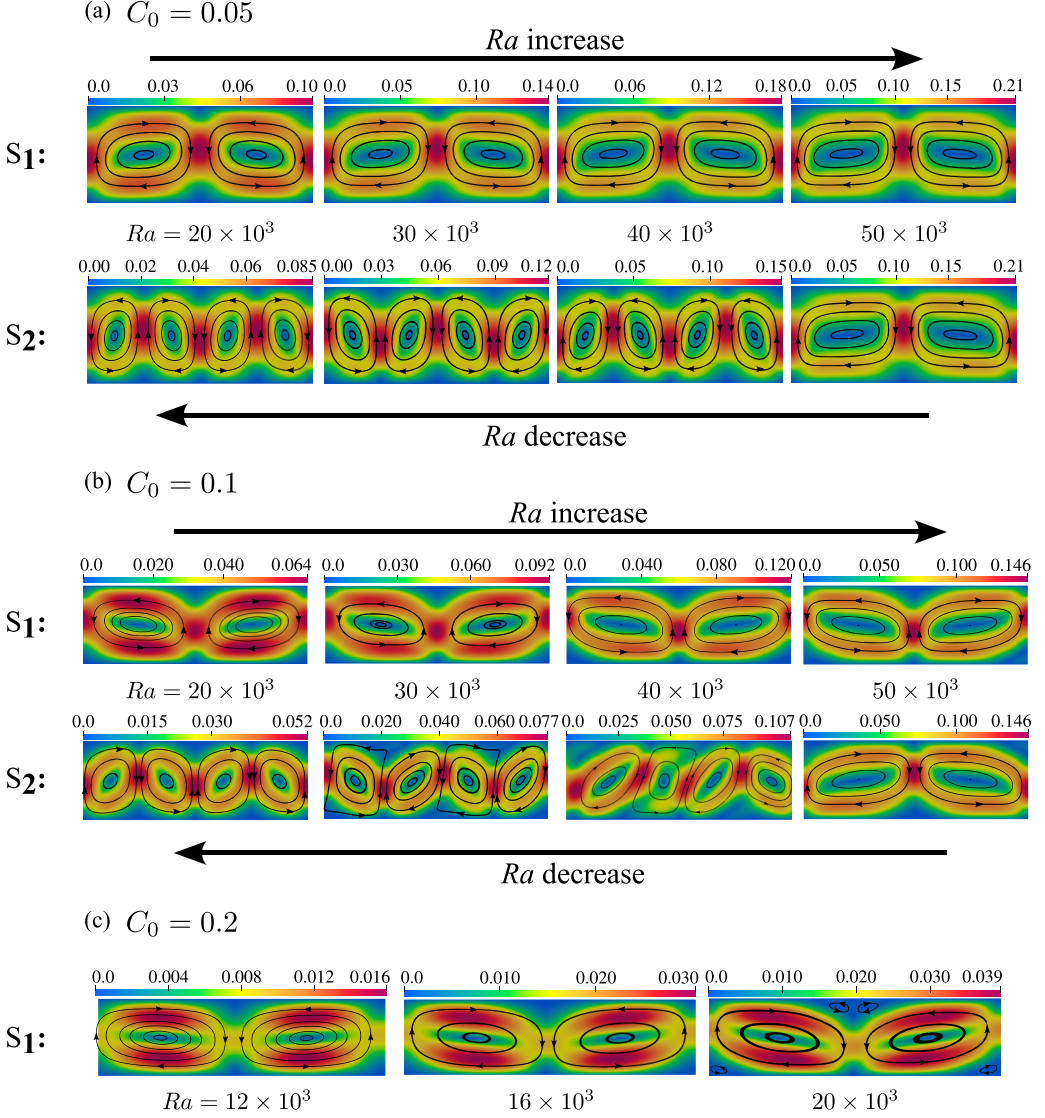


FIG. 7. Electroconvective flow patterns observed in solution branches S_1 and S_2 at $12 \times 10^3 \leq Ra \leq 50 \times 10^3$ for (a) $C_0 = 0.05$, (b) $C_0 = 0.1$, and (c) $C_0 = 0.2$.

the formation of secondary vortices at $Ra = 20 \times 10^3$. At this point, both the values of C_0 and Ra are high. The competition between the stabilizing electric field and the destabilizing thermal field lead to evolution of small secondary vortices near the peripheries of the primary vortices. With a further increase of Ra , this competition is intensified, and the flow enters an unsteady regime.

To further enunciate the flow features of RBC under the stabilizing effect of Onsager-Wien effect, the temporal evolution of U_{\max} at different values of Ra and at $C_0 = 0.05, 0.1$, and 0.2 are presented in Figs. 8(a) ~ 8(c), respectively. In all the cases, the maximum velocity magnitude is an increasing function of Ra . In general, the peak velocity remains zero briefly at the start of the simulations, as the simulations are initialized with zero fields for all variables. After the initial dormant period, the U_{\max} curve shows a momentary spike and then slowly reaches a steady state. The initial dormant period is longer for smaller values of Ra . The magnitude of U_{\max} is lower at higher values C_0 ,

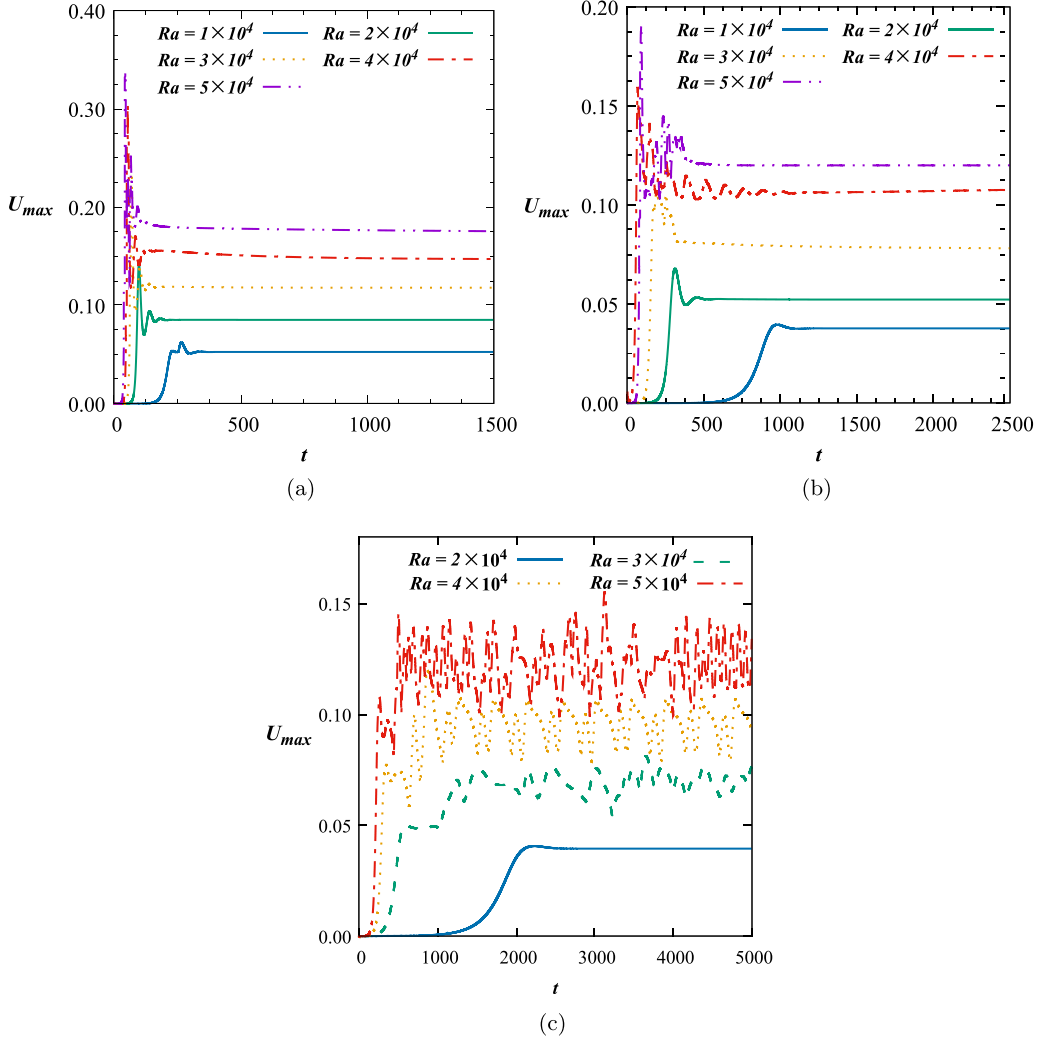


FIG. 8. Temporal variations of maximum velocity U_{max} at different Rayleigh numbers (Ra) and different conduction numbers (a) $C_0 = 0.05$, (b) $C_0 = 0.1$, and (c) $C_0 = 0.2$.

indicating the inability of the buoyancy force to overcome the stronger electric force at higher C_0 . As explained earlier, the competition between the electric and buoyancy forces leads to unsteady flow at $C_0 = 0.2$ with higher values of Ra . Thus, higher values of Ra at $C_0 = 0.2$ are characterized by periodic oscillations of U_{max} with respect to time. The randomness and amplitude of the oscillations increase with increasing values of Ra . The contours of distribution of nondimensional physical variables: negative-charge density N_p , positive-charge density N_n , electric field \mathbf{E} , and electric force \mathbf{F}_e are presented in Fig. 9. The contours correspond to $C_0 = 0.1$, $Ra = 20 \times 10^3$ with zero-field initialization. The heterocharge layer formation near the plate electrodes is seen in the contours of charge densities. The negative charges have accumulated near the bottom high-voltage electrode and vice versa. Due to the accumulation of charges close to the oppositely charged electrodes, the maximum intensity of electric force is observed near the electrodes. The distributions of N_p , N_n , \mathbf{E} , and y component of \mathbf{F}_e along a vertical line $x = 0.5$ are presented in Figs. 10(a) ~ 10(d), respectively. At all values of C_0 , the highest values of charge density distribution are noted near

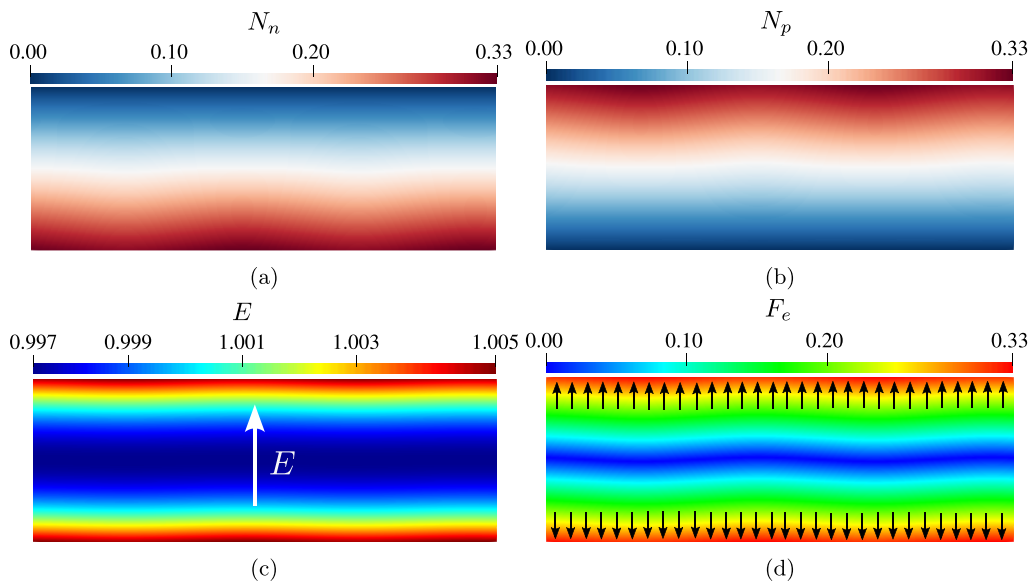


FIG. 9. Distribution of (a) Negative-charge distribution (N_n), (b) Positive-charge distribution (N_p), (c) Electric field (\mathbf{E}), and (d) Electric force (\mathbf{F}_e) at $C_0 = 0.1$ and $Ra = 20 \times 10^3$ with zero-field initialization.

the oppositely charged electrodes. The positive-charge intensity is lowest near the bottom high-voltage electrode, linearly increases in the vertical direction, and reaches the maximum value near the top grounded electrode. Likewise, the negative-charge density is highest near the bottom high-voltage electrode and linearly decreases toward the lowest value near the top grounded electrode. The electric field intensity has peak values near both the electrodes and the lowest value in the midpoint of the line $x = 0.5$. Both the maximum and minimum values of \mathbf{E} are noted at $C_0 = 0.2$. The electric force is in the downward direction near the bottom electrode and is in the upward direction near the top electrode. The electric force is stronger near the electrodes and weaker in the central region.

D. Heat transfer characteristics with electro-thermo-convection

The heat transfer characteristics associated with the flow at different combinations of C_0 and Ra are presented in this section. The variation of mean Nusselt number (Nu) along the hot bottom wall at varying Ra and $C_0 = 0.05, 0.1$ and 0.2 are presented in Figs. 11(a) ~ 11(c). Irrespective of the value of C_0 , the mean Nusselt number Nu increases with the increase of Ra . Similar to Fig. 6, the points marked with red color can be obtained by initializing the simulations both by zero-field values or the solutions from the previous convective states. The yellow colored points can only be obtained by simulations initialized with solution from the preceding convective state. For $C_0 = 0.05$ and 0.1 , we observe two solution branches, S_1 (upper branch) and S_2 (lower branch). As observed in Fig. 6, the upper branches (S_1) are marked with solid lines; the values of Nu correspond to a flow structure with single pair of vortices. However, the lower solution branch (S_2) marked with dotted lines correspond to Nu values for the flow structure with two pairs of vortices. The lower values of Nu observed in S_2 can be attributed to the comparatively lower velocity distributions observed in the S_2 branch (refer Fig. 7). Unlike the cases of $C_0 = 0.05$ and 0.1 , the case with $C_0 = 0.2$ requires a much higher value of Ra_c for the onset of fluid motion, and also, the resultant flow intensity is lower when compared to that in $C_0 = 0.05$ and 0.1 . The comparatively weaker flow in $C_0 = 0.2$ leads to a lesser increase in heat transfer. Thus, the values of Nu noted at $C_0 = 0.2$ are lower than that observed in $C_0 = 0.05$ and 0.1 . The contours of temperature distribution in solution

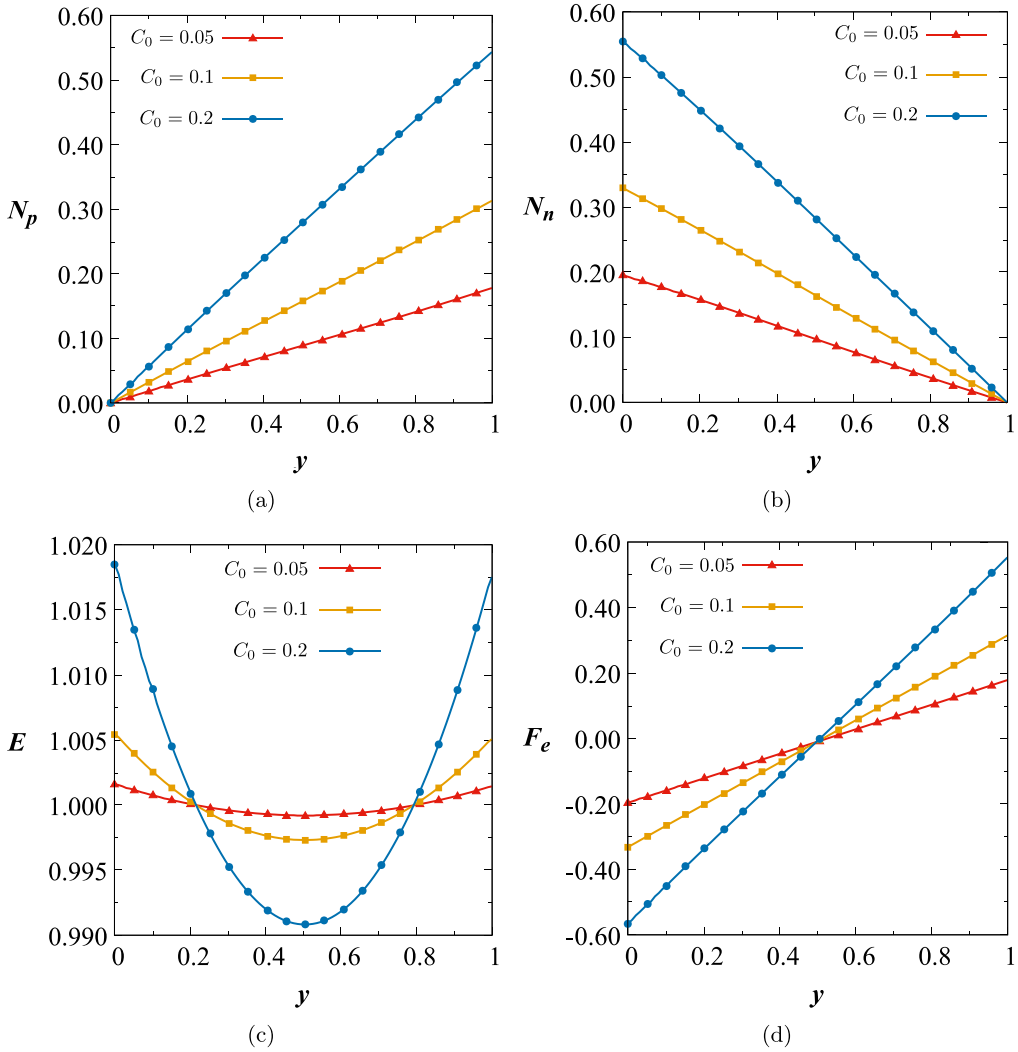


FIG. 10. Variation of the physical quantities in the hydrodynamic state at Rayleigh number $Ra = 10^4$ and different conduction numbers C_0 along a vertical line $x = 0.5$. (a) Positive-charge density (N_p), (b) Negative-charge density (N_n), (c) Electric field (\mathbf{E}), and (d) y component of electric force (\mathbf{F}_e).

branches S_1 and S_2 observed at $0.05 \leq C_0 \leq 0.2$ and $12 \times 10^3 \leq Ra \leq 50 \times 10^3$ are presented in Fig. 12. At $C_0 = 0.05$, the solution branches S_1 correspond to the bicellular flow structure. A single mushroom-shaped vertical thermal plume at the center of the domain characterizes the thermal field. The solution branch S_2 at $C_0 = 0.05$ marks a shift from bicellular flow to a structure with four cells (two pairs of vortices). This flow pattern leads to a thermal field with two vertical mushroom-shaped thermal plumes located in the region between the vortices (refer Fig. 7). The case of $C_0 = 0.1$ also shows two solution branches, S_1 and S_2 , with bicellular and multicellular (four cells) flow structures, respectively. Correspondingly, single- and two-thermal-plume structures are noted at S_1 and S_2 . However, the thermal plumes in S_2 are not perfectly vertical owing to the asymmetric flow structure (refer Fig. 7). The case of $C_0 = 0.2$ has only one solution branch. In this case, the mushroom-shaped thermal plumes are not fully developed due to the weak velocity distribution, as noted in Fig. 7.

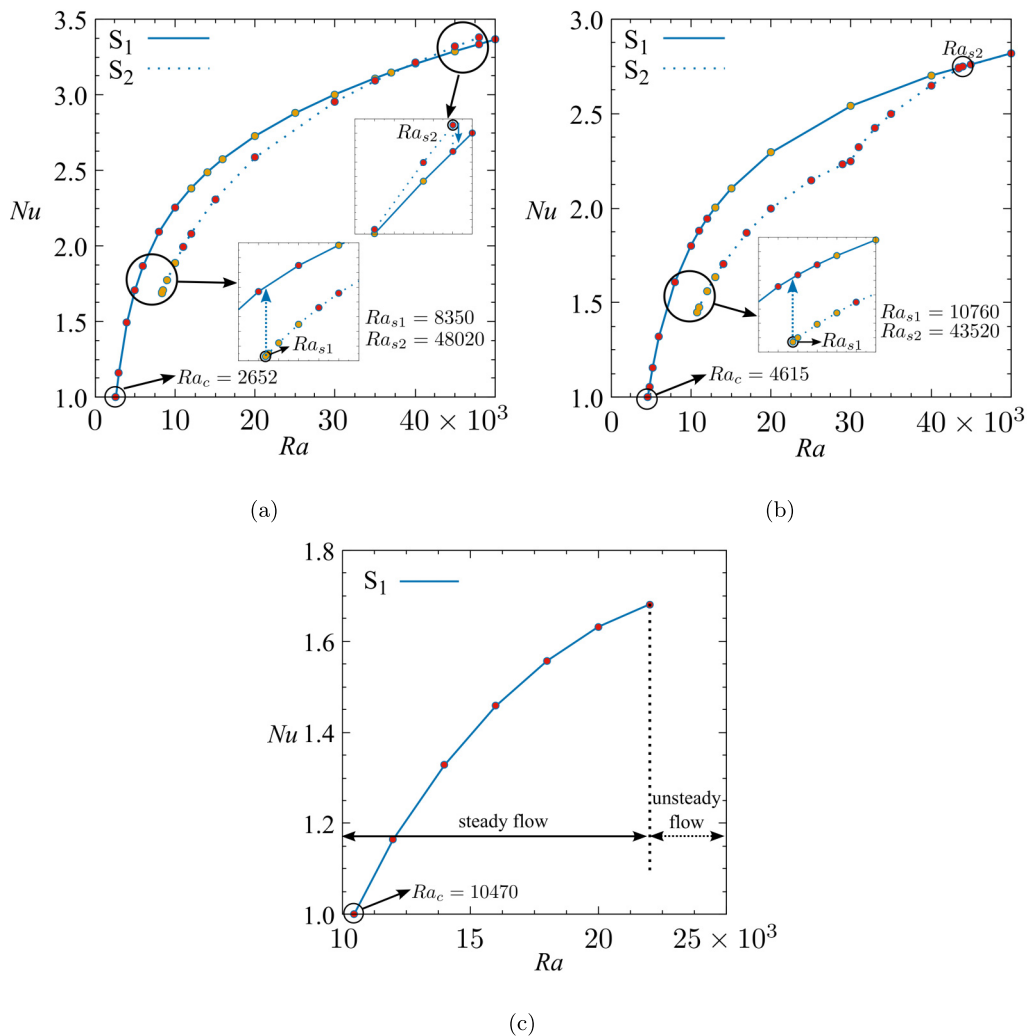


FIG. 11. Variation of mean Nusselt number Nu with respect to Rayleigh number Ra at different values of conduction numbers (a) $C_0 = 0.05$, (b) $C_0 = 0.1$, and (c) $C_0 = 0.2$. (S_1 and S_2 represent the flow pattern of a pair of vortices and two pairs of vortices, respectively.)

V. CONCLUDING REMARKS

A combined stability and numerical analysis of Rayleigh-Bénard convection with Onsager-Wien effect in a planar dielectric liquid layer is presented. For the first time in literature, flow instability of of Rayleigh-Bénard convection in a dielectric liquid layer under the stabilizing effect of Onsager-Wien effect occurring at weak and medium electric fields is studied. Combined effects of control parameters Rayleigh number Ra and conduction number C_0 are considered. At first, solutions for the physical variables at the hydrostatic regime are derived with Newton's method. Then, modal stability analysis is performed to identify the critical Rayleigh number Ra_c concerning different conduction numbers. In the configuration considered in this study, the electric force stabilizes the liquid layer, while the buoyancy force attempts to destabilize the layer. A neutral stability curve in the Ra - C_0 plane is obtained, and higher conduction number C_0 values correspond to higher values of Ra_c . This indicates that a more potent buoyancy force is required to overcome the stabilizing

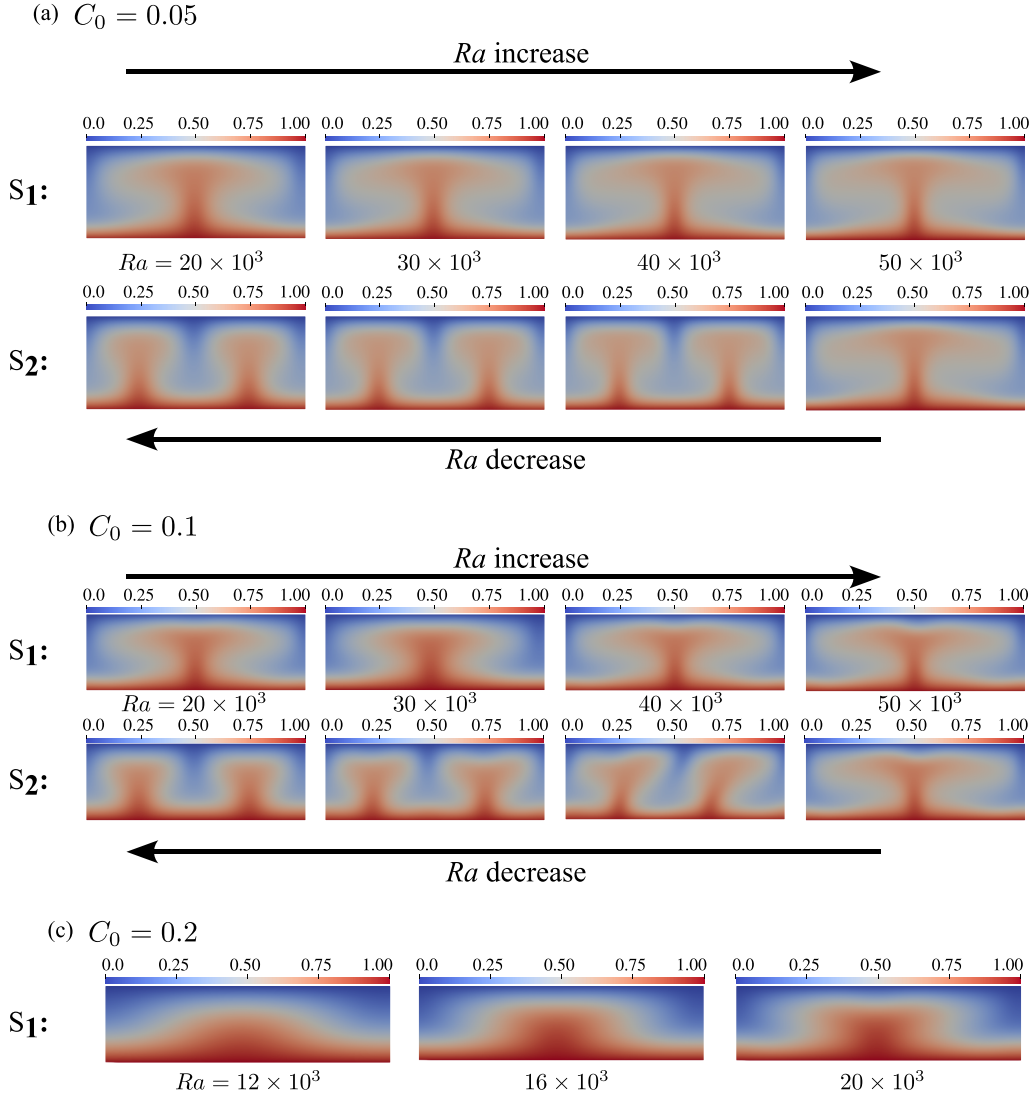


FIG. 12. Thermal field visualization in solution branches S_1 and S_2 at $12 \times 10^3 \leq Ra \leq 50 \times 10^3$ for (a) $C_0 = 0.05$, (b) $C_0 = 0.1$, and (c) $C_0 = 0.2$.

effect of electric force at higher C_0 . The values of Ra_C obtained by the numerical simulations agree with those obtained by the modal stability analysis. Finally, extensive numerical simulations are performed to study the flow and heat transfer characteristics with different combinations of control parameters. At $C_0 = 0.05$ and 0.1 , the problem exhibits dual solutions depending on the initialization method. The resultant flow morphology is characterized by two or four flow vortices depending on zero-field or previous convective state initialization, respectively. Thus, two solution branches exist in the bifurcation diagram depending on the initialization method. The mechanism of destabilization of the fluid layer under the combined action of buoyancy and electric forces is discussed. The velocity distribution and heat transfer are generally higher at lower values of C_0 and higher values of Ra . Owing to the intensified competition between the stabilizing electric field and the destabilizing thermal field, at higher values of Ra and at $C_0 = 0.2$, the flow exhibits an unsteady behavior. The present study aids in understanding the flow and heat transfer behavior observed in

a combined Rayleigh-Bénard convection and Onsager-Wien effect (under a weak/medium electric field). Results presented herein will help in the design of engineering flow systems that are subjected to combined gradients of thermal and electric fields.

ACKNOWLEDGMENTS

We are very grateful for the guidance offered by Zhen Ouyang and Zhiwei Song on the Newton's method and modal stability analysis. This work is supported by the National Natural Science Foundation of China (Grant No. 12172110), the National Key Research and Development Program of China (Grant No. 2020YFC2201004) and the Fundamental Research Funds for Central Universities (Grant No. AUGA9803500921).

-
- [1] R. Kelly and H. Hu, The onset of Rayleigh-Bénard convection in nonplanar oscillatory flows, *J. Fluid Mech.* **249**, 373 (1993).
 - [2] A. Or and R. Kelly, The effects of thermal modulation upon the onset of Marangoni-Bénard convection, *J. Fluid Mech.* **456**, 161 (2002).
 - [3] Y.-B. Hu, S.-D. Huang, Y.-C. Xie, and K.-Q. Xia, Centrifugal-force-induced flow bifurcations in turbulent thermal convection, *Phys. Rev. Lett.* **127**, 244501 (2021).
 - [4] C. Kang, H. N. Yoshikawa, and P. Mirbod, Onset of thermal convection in noncolloidal suspensions, *J. Fluid Mech.* **915**, A128 (2021).
 - [5] P. Bergé and M. Dubois, Rayleigh-Bénard convection, *Contemp. Phys.* **25**, 535 (1984).
 - [6] E. Bodenschatz, W. Pesch, and G. Ahlers, Recent developments in Rayleigh-Bénard convection, *Annu. Rev. Fluid Mech.* **32**, 709 (2000).
 - [7] X. Zhu, V. Mathai, R. J. A. M. Stevens, R. Verzicco, and D. Lohse, Transition to the ultimate regime in two-dimensional Rayleigh-Bénard convection, *Phys. Rev. Lett.* **120**, 144502 (2018).
 - [8] D. Puigjaner, J. Herrero, C. Simo, and F. Giralt, Bifurcation analysis of steady Rayleigh-Bénard convection in a cubical cavity with conducting sidewalls, *J. Fluid Mech.* **598**, 393 (2008).
 - [9] G. Ahlers, E. Bodenschatz, R. Hartmann, X. He, D. Lohse, P. Reiter, R. J. A. M. Stevens, R. Verzicco, M. Wedi, S. Weiss *et al.*, Aspect ratio dependence of heat transfer in a cylindrical Rayleigh-Bénard cell, *Phys. Rev. Lett.* **128**, 084501 (2022).
 - [10] S. Chandrasekhar, The instability of a layer of fluid heated below and subject to the simultaneous action of a magnetic field and rotation, *Proc. R. Soc. London A* **225**, 173 (1954).
 - [11] S. Chandrasekhar, The instability of a layer of fluid heated below and subject to the simultaneous action of a magnetic field and rotation II., *Proc. R. Soc. London A* **237**, 476 (1956).
 - [12] J. C. Yang, T. Vogt, and S. Eckert, Transition from steady to oscillating convection rolls in Rayleigh-Bénard convection under the influence of a horizontal magnetic field, *Phys. Rev. Fluids* **6**, 023502 (2021).
 - [13] J. Song, P. Li, L. Chen, C. Li, B. Li, and L. Huang, A review on Rayleigh-Bénard convection influenced by the complicating factors, *Int. Commun. Heat Mass Transfer* **144**, 106784 (2023).
 - [14] P. Traoré, A. T. Pérez, D. Koulova, and H. Romat, Numerical modelling of finite-amplitude electrothermo-convection in a dielectric liquid layer subjected to both unipolar injection and temperature gradient, *J. Fluid Mech.* **658**, 279 (2010).
 - [15] F. McCluskey, P. Atten, and A. Perez, Heat transfer enhancement by electroconvection resulting from an injected space charge between parallel plates, *Int. J. Heat Mass Transf.* **34**, 2237 (1991).
 - [16] M. Gao, L. Zhang, D. Zhang, and L. Zhang, Experimental study on the enhancement of free convection heat transfer under the action of an electric field, *Exp. Therm. Fluid Sci.* **104**, 9 (2019).
 - [17] Z. Lu, G. Liu, and B. Wang, Flow structure and heat transfer of electro-thermo-convection in a dielectric liquid layer, *Phys. Fluids* **31**, 064103 (2019).
 - [18] R. D. Selvakumar, J. Wu, J. Huang, and P. Traoré, Electro-thermo-convection in a differentially heated square cavity under arbitrary unipolar injection of ions, *Int. J. Heat Fluid Flow* **89**, 108787 (2021).

- [19] Q. Wang, Y. Guan, T. Wei, and J. Wu, Transition sequences and heat transfer enhancement in electrothermo-convection of a dielectric liquid between two parallel electrodes, *Int. J. Therm. Sci.* **179**, 107705 (2022).
- [20] Y. Zhang, H. Jiang, K. Luo, T. Li, J. Wu, and H. Yi, Electro-thermo-convection in a high prandtl number fluid: Flow transition and heat transfer, *Int. J. Heat Mass Transf.* **201**, 123630 (2023).
- [21] A. Castellanos, *Electrohydrodynamics*, Vol. 380 (Springer Science & Business Media, Berlin, 1998).
- [22] J. Wu, P. Traoré, A. T. Pérez, and P. A. Vázquez, On two-dimensional finite amplitude electro-convection in a dielectric liquid induced by a strong unipolar injection, *J. Electrostat.* **74**, 85 (2015).
- [23] B. Kim, S. Lee, Y. S. Lee, and K. H. Kang, Ion wind generation and the application to cooling, *J. Electrostat.* **70**, 438 (2012).
- [24] P. Atten and R. Moreau, Stabilité électrohydrodynamique des liquides isolants soumis à une injection unipolaire, *J. Mécanique* **11**, 471 (1972).
- [25] M. Zhang, F. Martinelli, J. Wu, P. J. Schmid, and M. Quadrio, Modal and nonmodal stability analysis of electrohydrodynamic flow with and without cross-flow, *J. Fluid Mech.* **770**, 319 (2015).
- [26] W. J. Worraker and A. T. Richardson, A nonlinear electrohydrodynamic stability analysis of a thermally stabilized plane layer of dielectric liquid, *J. Fluid Mech.* **109**, 217 (1981).
- [27] M. Zhang, Weakly nonlinear stability analysis of subcritical electrohydrodynamic flow subject to strong unipolar injection, *J. Fluid Mech.* **792**, 328 (2016).
- [28] J. M. Schneider and P. K. Watson, Electrohydrodynamic stability of space-charge-limited currents in dielectric liquids. I. Theoretical study, *Phys. Fluids* **13**, 1948 (1970).
- [29] P. Atten and J. C. Lacroix, Non-linear hydrodynamic stability of liquids subjected to unipolar injection, *J. Mec.* **18**, 469 (1979).
- [30] E. D. Fylladitakis, M. P. Theodoridis, and A. X. Moronis, Review on the history, research, and applications of electrohydrodynamics, *IEEE Trans. Plasma Sci.* **42**, 358 (2014).
- [31] P. Atten and J. Seyed-Yagoobi, Electrohydrodynamically induced dielectric liquid flow through pure conduction in point/plane geometry, *IEEE Trans. Dielectr. Electr. Insul.* **10**, 27 (2003).
- [32] M. R. Pearson and J. Seyed-Yagoobi, Advances in electrohydrodynamic conduction pumping, *IEEE Trans. Dielectr. Electr. Insul.* **16**, 424 (2009).
- [33] M. A. Siddiqui and J. Seyed-Yagoobi, Experimental study of pumping of liquid film with electric conduction phenomenon, *IEEE Trans. Ind. Appl.* **45**, 3 (2009).
- [34] Y. Feng and J. Seyed-Yagoobi, Understanding of electrohydrodynamic conduction pumping phenomenon, *Phys. Fluids* **16**, 2432 (2004).
- [35] S.-I. Jeong and J. Seyed-Yagoobi, Innovative electrode designs for electrohydrodynamic conduction pumping, *IEEE Trans. Ind. Appl.* **40**, 900 (2004).
- [36] M. Yazdani and J. Seyed-Yagoobi, Effect of charge mobility on dielectric liquid flow driven by EHD conduction phenomenon, *J. Electrostat.* **72**, 285 (2014).
- [37] P. Vázquez, M. Talmor, J. Seyed-Yagoobi, P. Traoré, and M. Yazdani, In-depth description of electrohydrodynamic conduction pumping of dielectric liquids: Physical model and regime analysis, *Phys. Fluids* **31**, 113601 (2019).
- [38] R. D. Selvakumar, D. Zhonglin, and J. Wu, Heat transfer intensification by EHD conduction pumping for electronic cooling applications, *Int. J. Heat Fluid Flow* **95**, 108972 (2022).
- [39] J. Wu, P. Traoré, A. T. Pérez, and M.-Q. Zhang, Numerical analysis of the subcritical feature of electro-thermo-convection in a plane layer of dielectric liquid, *Physica D* **311-312**, 45 (2015).
- [40] K. Luo, J. Wu, H. Yi, and H. Tan, Lattice boltzmann modelling of electro-thermo-convection in a planar layer of dielectric liquid subjected to unipolar injection and thermal gradient, *Int. J. Heat Mass Transf.* **103**, 832 (2016).
- [41] Z. Su, T. Li, W. Su, and H. Yi, Numerical simulation of electrothermal convection in dielectric liquids enclosed within rectangular cavities, *Fluid Dyn.* **56**, 922 (2021).
- [42] Y. Peng, Q. Liu, Z. Li, and J. Wu, Finite amplitude electro-thermo convection in a cubic box, *Fluid Dynam. Res.* **54**, 065501 (2022).

- [43] Y. Guan, X. He, Q. Wang, Z. Song, M. Zhang, and J. Wu, Monotonic instability and overstability in two-dimensional electrothermohydrodynamic flow, *Phys. Rev. Fluids* **6**, 013702 (2021).
- [44] A. Mordvinov and B. Smorodin, Electroconvection under injection from cathode and heating from above, *J. Exp. Theor. Phys.* **114**, 870 (2012).
- [45] P. Atten, F. McCluskey, and A. Perez, Electroconvection and its effect on heat transfer, *IEEE Trans. Electr. Insul.* **23**, 659 (1988).
- [46] T. B. Jones, Electrohydrodynamically enhanced heat transfer in liquids—A review, *Adv. Heat Transfer* **14**, 107 (1979).
- [47] J. L. Lara, F. Pontiga, and A. Castellanos, Stability analysis of a Taylor–Couette flow of insulating fluid subjected to radial unipolar injection of charge, *Phys. Fluids* **10**, 3088 (1998).
- [48] P. Langevin, Recombinaison et mobilités des ions dans les gaz, *Ann. Chim. Phys.* **28**, 122 (1903).
- [49] D. Fernandes, D. Cho, and Y. Suh, Electrohydrodynamic flow of dielectric liquid around a wire electrode—effect of truncation of Onsager function, *IEEE Trans. Dielectr. Electr. Insul.* **21**, 194 (2014).
- [50] M. Darwish and F. Moukalled, *The Finite Volume Method in Computational Fluid Dynamics: An Advanced Introduction with OpenFOAM and Matlab* (Springer, New York, NY, 2016).
- [51] B. Leonard, Order of accuracy of quick and related convection-diffusion schemes, *Appl. Math. Model.* **19**, 640 (1995).
- [52] B. van Leer, Towards the ultimate conservative difference scheme. V. A second-order sequel to Godunov’s method, *J. Comput. Phys.* **32**, 101 (1979).
- [53] J. Wu and P. Traoré, A finite-volume method for electro-thermoconvective phenomena in a plane layer of dielectric liquid, *Numer. Heat Transfer, Part A* **68**, 471 (2015).
- [54] N. Nourdanesh, S. Hossainpour, and K. Adamiak, Numerical simulation and optimization of natural convection heat transfer enhancement in solar collectors using electrohydrodynamic conduction pump, *Appl. Therm. Eng.* **180**, 115825 (2020).
- [55] M. Mirzaei and M. Saffar-Avval, Enhancement of convection heat transfer using EHD conduction method, *Exp. Therm. Fluid Sci.* **93**, 108 (2018).
- [56] R. Gharraei, M. Hemayatkhah, S. B. Islami, and E. Esmailzadeh, An experimental investigation on the developing wavy falling film in the presence of electrohydrodynamic conduction phenomenon, *Exp. Therm. Fluid Sci.* **60**, 35 (2015).
- [57] R. L. Burden, J. D. Faires, and A. M. Burden, *Numerical Analysis* (Cengage Learning, Boston, MA, 2015).
- [58] L. N. Trefethen, *Spectral Methods in MATLAB* (SIAM, Philadelphia, PA, 2000).
- [59] F. Pontiga and A. Castellanos, The onset of electrothermal convection in nonpolar liquids on the basis of a dissociation-injection conductivity model, *IEEE Trans. Ind. Appl.* **28**, 520 (1992).
- [60] J. W. Eaton, D. Bateman, S. Hauberg, and R. Wehbring, GNU Octave Version 5.2.0 Manual: A High-level Interactive Language for Numerical Computations (2020), <https://docs.octave.org/v5.2.0/>.
- [61] F. Pontiga and A. Castellanos, Physical mechanisms of instability in a liquid layer subjected to an electric field and a thermal gradient, *Phys. Fluids* **6**, 1684 (1994).